

Damping of slow surface sausage modes in photospheric waveguides

Shao-Xia Chen¹

Bo Li¹

bbl@sdu.edu.cn

Mijie Shi¹

and

Hui Yu¹

ABSTRACT

There has been considerable interest in sausage modes in photospheric waveguides like pores and sunspots, and slow surface sausage modes (SSSMs) have been suggested to damp sufficiently rapidly to account for chromospheric heating. Working in the framework of linear resistive magnetohydrodynamics, we examine how efficient electric resistivity and resonant absorption in the cusp continuum can be for damping SSSMs in a photospheric waveguide with equilibrium parameters compatible with recent measurements of a photospheric pore. For SSSMs with the measured wavelength, we find that the damping rate due to the cusp resonance is substantially less strong than theoretically expected with the thin-boundary approximation. The damping-time-to-period ratio (τ/P) we derive for standing modes, equivalent to the damping-length-to-wavelength ratio for propagating modes given the extremely weak dispersion, can reach only ~ 180 . However, the accepted values for electric resistivity (η) correspond to a regime where both the cusp resonance and resistivity play a role. The values for τ/P attained at the largest allowed η may reach ~ 30 . We conclude that electric resistivity can be considerably more efficient than the cusp resonance for damping SSSMs in the pore in question, and it needs to be incorporated into future studies on the damping of SSSMs in photospheric waveguides in general.

Subject headings: magnetohydrodynamics (MHD) — Sun: photosphere — Sun: magnetic fields — waves

¹Shandong Provincial Key Laboratory of Optical Astronomy and Solar-Terrestrial Environment, Institute of Space Sciences, Shandong University, Weihai 264209, China

1. INTRODUCTION

Identifying magnetohydrodynamic (MHD) waves in the structured solar atmosphere is vital from the perspectives of both solar magneto-seismology (SMS, see recent reviews by, e.g., Nakariakov & Verwichte 2005; De Moortel & Nakariakov 2012; Nakariakov et al. 2016) and atmospheric heating (see e.g., Arregui 2015; De Moortel & Browning 2015, for recent reviews). While coronal waves and oscillations remain a focus (Aschwanden et al. 1999; Nakariakov et al. 1999; Wang et al. 2002; Ofman & Wang 2008; Erdélyi & Taroyan 2008; Verwichte et al. 2009; Aschwanden & Schrijver 2011; Pascoe et al. 2016, to name only a few), various MHD modes have also been identified in a considerable number of structures in the lower solar atmosphere (e.g., De Pontieu et al. 2007, Jess et al. 2009, He et al. 2009, Morton et al. 2012, Tian et al. 2014, Jess et al. 2017, Wang et al. 2018; see also the review by Arregui et al. 2012 and references therein). In particular, photospheric pores and sunspots were shown to host a variety of waves. Thanks to modern high-cadence and high-spatial-resolution instruments like the Rapid Oscillations in the Solar Atmosphere (ROSA, Jess et al. 2010), these waves were ascertained, on the bases of parity and axial phase speed, to be either fast or slow sausage waves (Dorotovič et al. 2008; Morton et al. 2011; Dorotovič et al. 2014; Moreels et al. 2015; Grant et al. 2015; Freij et al. 2016). More recently, the measurements of the spatial distribution of wave power enabled these waves to be further grouped into surface and body modes (Keys et al. 2018).

Among the above-mentioned studies on waves in photospheric structures, of particular interest are the recent multi-wavelength measurements of slow surface sausage modes (SSSMs) in a magnetic pore, where propagating SSSMs were shown to damp over a length-scale as short as a quarter of the wavelength so as to be important in heating the chromosphere (Grant et al. 2015, hereafter G15). Working with the thin-boundary (TB) approximation, Yu et al. (2017b, hereafter Y17; also Yu et al. 2017a) showed that the resonant absorption of SSSMs in the cusp continuum may play a substantial role in their damping, with the damping-time-to-period ratio (τ/P) attaining down to ~ 10 . Note that while this damping was obtained for standing modes (i.e., real axial wavenumbers), the damping-length-to-wavelength ratio (L_D/λ) is nearly identical to τ/P because of the extremely weak dispersion of SSSMs. Note further that even though the theoretical framework in the TB limit was well-established (see the review by Goossens et al. 2011, and references therein), Y17 were the first to show that the cusp resonance of SSSMs is stronger than thought, even though the values of L_D/λ are not sufficient to account for the measured heavy damping.

The purpose of this study is to further examine the damping of SSSMs in photospheric waveguides by solving the linearized resistive MHD equations. By so doing, we will address how efficient the damping due to the cusp resonance is in a more general sense where the TB

approximation is not invoked. In addition, we will also be able to assess the role of electric resistivity (η) for damping SSSMs. This latter point is important in that the magnetic Reynolds numbers (R_m) in pores and sunspots may be orders-of-magnitude smaller than typical coronal values ($\sim 10^{12} - 10^{14}$). Take the pore examined by G15, for which the radius $R \sim 1500$ km and the internal Alfvén speed $v_{Ai} \sim 12$ km s $^{-1}$. For electric conductivity ($\sigma = 1/\eta$), we quote values in the range between 1.3 and 420 S m $^{-1}$, which were in fact derived by [Kovitya & Cram \(1983\)](#) for a model sunspot umbra in the temperature range of 3500 to ~ 6400 K. One finds a range between 3×10^4 and 10^7 for R_m as defined by $\mu_0 \sigma R v_{Ai}$, where μ_0 is the magnetic permeability in free space.¹ As is well-known, resonant absorption is essentially an ideal MHD process whereby the attenuation of the collective modes is due to their energy being transferred to localized waves (either Alfvén or slow or both), even though these localized waves are eventually dissipated. From the perspective of resistive MHD, the associated damping rates can be found from the eigen-frequencies ω at sufficiently large R_m such that ω is independent of R_m (see e.g., [Poedts & Kerner 1991](#); [Van Doorselaere et al. 2004](#); [Terradas et al. 2006](#); [Guo et al. 2016](#), for kink waves resonantly coupled to the Alfvén continuum). However, it is not known a priori whether the above-quoted R_m is sufficiently large. So in short, we would like to address two questions: One, what happens to the damping rate due to the cusp resonance if the waveguide boundary is not thin? Second, how does the damping efficiency due to direct resistive dissipation compare with that associated with the cusp resonance? Our problem formulation is given in [Section 2](#) and the numerical results are presented in [Section 3](#). [Section 4](#) summarizes this study and ends with some concluding remarks.

2. MATHEMATICAL FORMULATION

With magnetic pores in mind, we model photospheric waveguides as static, straight magnetic cylinders aligned with the equilibrium magnetic field $\mathbf{B}_0 = B_0 \hat{z}$ in a cylindrical coordinate system (r, θ, z) . We neglect gravity throughout, and hence the equilibrium parameters (denoted by subscript 0) depend only on r . Let ρ , p , and \mathbf{v} denote mass density, thermal pressure, and velocity, respectively. The adiabatic sound speed c_s , Alfvén speed v_A , and cusp (or tube) speed c_T are defined by the equilibrium values as

$$c_s^2 = \frac{\gamma p_0}{\rho_0}, \quad v_A^2 = \frac{B_0^2}{\mu_0 \rho_0}, \quad c_T^2 = \frac{c_s^2 v_A^2}{c_s^2 + v_A^2}, \quad (1)$$

¹The range of electric conductivity is also compatible with, e.g., [Wang \(1993, Fig. 1\)](#) and [Khomenko & Collados \(2012, Fig. 1\)](#), see also [Ni et al. \(2016\)](#). Note that the resistivity we address corresponds to the classical Ohmic one using the terminology of [Khomenko & Collados \(2012\)](#).

where $\gamma = 5/3$ is the adiabatic index. The transverse distribution of the equilibrium parameters is assumed to comprise a uniform cord (denoted by subscript i), a uniform external medium (subscript e), and a continuous transition layer (TL) connecting the two. To realize this, we assume that c_T^2 and c_s^2 in the TL are given by

$$\mathcal{E}_{\text{TL}}(r) = \frac{\mathcal{E}_i + \mathcal{E}_e}{2} - \frac{\mathcal{E}_i - \mathcal{E}_e}{2} \sin \frac{\pi(r - R)}{l}, \quad (2)$$

which applies for $R - l/2 \equiv r_i \leq r \leq r_e \equiv R + l/2$. Here \mathcal{E} represents c_T^2 and c_s^2 , R denotes the mean radius, and l the TL width. Identical to [Edwin & Roberts \(1983\)](#), we take $[c_{\text{si}}, c_{\text{se}}, v_{\text{Ae}}] = [0.5, 0.75, 0.25]v_{\text{Ai}}$, resulting in $[c_{\text{Ti}}, c_{\text{Te}}] = [0.4472, 0.2372]v_{\text{Ai}}$. If taking $v_{\text{Ai}} = 12 \text{ km s}^{-1}$, then one finds that $[c_{\text{si}}, c_{\text{se}}, v_{\text{Ae}}] = [6, 9, 3] \text{ km s}^{-1}$, largely compatible with G15 for the height range of $[0, 1000] \text{ km}$ (see their Fig. 4). Note that if we see R , ρ_i and v_{Ai} as normalizing constants, and once l/R is specified, then the equilibrium profile is complete as a result of transverse force balance, namely,

$$p_0 + \frac{B_0^2}{2\mu_0} = \rho_0 \left(\frac{c_s^2}{\gamma} + \frac{v_A^2}{2} \right) = \text{const}. \quad (3)$$

From the set of independent constants $[R, \rho_i, v_{\text{Ai}}]$, we derive the constant for normalizing magnetic field strength as $\sqrt{\mu_0 \rho_i v_{\text{Ai}}^2}$, which equals B_i by definition. Then the constants to normalize time and thermal pressure are R/v_{Ai} and $\rho_i v_{\text{Ai}}^2 = B_i^2/\mu_0$, respectively. [Figure 1](#) presents the transverse distributions of the relevant equilibrium parameters with l/R arbitrarily chosen to be 0.3 for illustration purposes. Both the characteristic speeds ([Figure 1a](#)) and the equilibrium fluid parameters ([Figure 1b](#)) are shown. With c_T^2 and c_s^2 specified by [Equation \(2\)](#), all the profiles show a monotonical dependence on r with the exception of the equilibrium density ρ_0 . If we prescribe, say, a linear dependence on r of the equilibrium density and pressure profiles, the cusp speed c_T may possess a nonmonotonical r -dependence and hence SSSMs may experience multiple resonances in the TL (see [Yu et al. 2017a](#) for an example). We choose the present procedure for specifying the equilibrium profiles to avoid this further complication.

Let \mathbf{v}_1 , p_1 and \mathbf{B}_1 denote the perturbations to velocity, pressure, and magnetic field, respectively. The small-amplitude perturbations to the equilibrium are then governed by the following set of linearized, resistive MHD equations

$$\rho_0 \frac{\partial \mathbf{v}_1}{\partial t} = -\nabla p_1 + \frac{(\nabla \times \mathbf{B}_0) \times \mathbf{B}_1}{\mu_0} + \frac{(\nabla \times \mathbf{B}_1) \times \mathbf{B}_0}{\mu_0}, \quad (4)$$

$$\frac{\partial \mathbf{B}_1}{\partial t} = \nabla \times \left(\mathbf{v}_1 \times \mathbf{B}_0 - \frac{\eta}{\mu_0} \nabla \times \mathbf{B}_1 \right), \quad (5)$$

$$\frac{\partial p_1}{\partial t} = -\mathbf{v}_1 \cdot \nabla p_0 - \gamma p_0 \nabla \cdot \mathbf{v}_1 + 2 \frac{(\gamma - 1)\eta}{\mu_0^2} (\nabla \times \mathbf{B}_1) \cdot (\nabla \times \mathbf{B}_0), \quad (6)$$

which are in dimensional form. The electric resistivity η is assumed to be uniform for simplicity. With our normalizing constants, the dimensionless form of Equations (4) to (6) differs from their dimensional form only in two aspects. First, μ_0 disappears in Equation (4). Second, η/μ_0 and η/μ_0^2 in Equations (5) and (6) are both replaced with $1/R_m$, where $R_m = \mu_0 R v_{\text{Ai}}/\eta$ is the magnetic Reynolds number.²

Focusing on sausage modes, we adopt the following ansatz for any perturbation

$$f_1(r, z; t) = \text{Re} \left\{ \tilde{f}(r) \exp[-i(\omega t - kz)] \right\}, \quad (8)$$

where ω is the complex-valued angular frequency and k the real-valued axial wavenumber. Only the equations governing \tilde{v}_r , \tilde{v}_z , \tilde{B}_r , \tilde{B}_z and \tilde{p} survive. To be specific, they read

$$\omega \tilde{v}_r = -\frac{B_0}{\rho_0} \left(k \tilde{B}_r + i \frac{d\tilde{B}_z}{dr} \right) - \frac{i \tilde{B}_z}{\rho_0} \frac{dB_0}{dr} - \frac{i}{\rho_0} \frac{d\tilde{p}}{dr}, \quad (9)$$

$$\omega \tilde{v}_z = \frac{i \tilde{B}_r}{\rho_0} \frac{dB_0}{dr} + \frac{k \tilde{p}}{\rho_0}, \quad (10)$$

$$\omega \tilde{B}_r = -k B_0 \tilde{v}_r + \frac{1}{R_m} \left(i \frac{d^2 \tilde{b}_r}{dr^2} + \frac{i}{r} \frac{d\tilde{b}_r}{dr} - ik^2 \tilde{b}_r - \frac{i \tilde{b}_r}{r^2} \right), \quad (11)$$

$$\omega \tilde{B}_z = -i \tilde{v}_r \frac{dB_0}{dr} - B_0 \left(i \frac{d\tilde{v}_r}{dr} + i \frac{\tilde{v}_r}{r} \right) + \frac{1}{R_m} \left(i \frac{d^2 \tilde{b}_z}{dr^2} + \frac{i}{r} \frac{d\tilde{b}_z}{dr} - ik^2 \tilde{b}_z \right), \quad (12)$$

$$\omega \tilde{p} = -c_s^2 \rho_0 \left(i \frac{d\tilde{v}_r}{dr} + i \frac{\tilde{v}_r}{r} - k \tilde{v}_z \right) - i \tilde{v}_r \frac{dp_0}{dr} + \frac{2(\gamma - 1)}{R_m} \frac{dB_0}{dr} \left(k \tilde{B}_r + i \frac{d\tilde{B}_z}{dr} \right), \quad (13)$$

which are in dimensionless form. These equations constitute a standard eigen-value problem (EVP) when supplemented with proper boundary conditions. At the cylinder axis ($r = 0$), the parity of sausage modes dictates that $\tilde{v}_r = \tilde{B}_r = 0$ and the r -derivatives of the rest vanish. Infinitely far from the cylinder, all dependent variables are zero. Taking $[l/R, kR, R_m]$ as free parameters, we then solve the EVP with the code PDE2D (Sewell 1988), which was first introduced to the solar context by Terradas et al. (2006). A nonuniform grid is set up for

² Strictly speaking, the equilibrium cannot stay static with a spatially varying B_0 given a finite resistivity. An equilibrium flow $\mathbf{v}_0 = v_0 \hat{r}$ is needed to counteract magnetic diffusion, where \hat{r} is the unit vector in the r -direction. However, balancing $\mathbf{v}_0 \times \mathbf{B}_0$ with $\eta \nabla \times \mathbf{B}_0/\mu_0$ yields that

$$\frac{v_0}{v_{\text{Ai}}} = \frac{1}{R_m} \frac{d \ln B_0}{dr/R}. \quad (7)$$

With $l/R \geq 0.01$ and $R_m \geq 10^4$ as we adopt, $|v_0|$ is $\lesssim 1.5 \times 10^{-2} v_{\text{Ai}}$ or 180 m s^{-1} in absolute terms.

r between 0 and r_M , where r_M is the outer boundary. A substantial number of grid points are deployed in the TL to resolve the possible oscillatory behavior therein. We place r_M at $50 R$, and make sure that further increasing r_M does not introduce any appreciable change to the computed eigen-frequencies (ω). In short, ω is then formally expressed as

$$\frac{\omega R}{v_{\text{Ai}}} = \mathcal{G} \left(kR, \frac{l}{R}, R_m \right) . \quad (14)$$

The wave period P and damping time τ are given by $P = 2\pi/\omega_R$ and $\tau = 1/|\omega_I|$, respectively. We also define the axial phase speed v_{ph} as ω_R/k , and the axial group speed v_{gr} as $d\omega_R/dk$. Here we use the shorthand notations $\omega_R = \text{Re}(\omega)$ and $\omega_I = \text{Im}(\omega)$.

The damping rates associated with the cusp resonance are also computed in the TB limit ($l/R \ll 1$). Analytical treatments in this limit yield a dispersion relation (DR) for surface sausage modes as given by Equation (27) in Y17, where resistivity is not explicitly involved. Note that the location (r_c) where the cusp resonance takes place is not known beforehand. We therefore solve the pertinent DR by iteration. For any given set of $[l/R, kR]$, we solve the DR for ω with an initial guess of r_c , and then locate r_c with the computed ω_R such that ω_R/k equals c_T . Correcting the guess for r_c , we repeat this process until convergence is met. These TB eigen-frequencies will be compared with those at sufficiently large R_m from our resistive computations, where l/R is allowed to be arbitrary. ³

3. NUMERICAL RESULTS

To start, Figure 2 shows the dependence on R_m of the damping-time-to-period ratio τ/P of slow surface sausage modes (SSSMs) for a number of combinations of $[l/R, kR]$ as labeled. We will come back to this figure later, for now it suffices to note that τ/P tends to increase with R_m and eventually levels off. These saturation values are then taken as the values of ω pertinent to resonant absorption for each pair of $[l/R, kR]$. By saturation, we mean that the change in τ/P does not exceed 1.5% for R_m between 10^9 and 10^{10} . It turns out that saturation is not guaranteed when either kR or l/R is sufficiently large even for R_m as large as 10^{10} (such a hint can be seen from the red dotted curve pertaining to $[l/R, kR] = [0.3, 2]$). Note that here we followed a rather stringent definition of “saturation”. Examining the red dotted curve in Figure 2, one sees that τ/P depends only rather weakly on R_m when

³ If we are interested only in the cusp resonance for transition layers not that thin, then we can adopt the Frobenius approach by Soler et al. (2013) who worked exclusively in ideal MHD. This approach yields an analytical DR whose validity is not restricted to the TB limit. However, we adopt the resistive MHD approach because we are interested also in whether resistivity plays a role in wave damping.

$R_m \gtrsim 3 \times 10^8$. However, that τ/P shows a clear dependence on resistivity for R_m as large as $\sim 10^8$ is quite different from what happens to standing kink modes resonantly coupled to the Alfvén continuum in typical coronal loops. In the latter case, typically τ/P becomes independent of resistivity when R_m exceeds $\sim 10^5$ (see e.g., Terradas et al. 2006, Fig. 2; Guo et al. 2016, Fig. 9) or 10^6 (e.g., Van Doorselaere et al. 2004, Fig. 3). We tentatively attribute the differences in the dependence of τ/P on resistivity to two factors. First, the equilibrium parameters in this study are very different from the coronal cases. This is particularly true for the ordering of the characteristic speeds in and outside the waveguide. Second, the axial wavenumbers themselves are quite different. To be more specific, $kR = 2$ for the red dotted curve in Figure 2, whereas kR is typically taken to be $\lesssim 0.1\pi$ in studies on standing kink modes in coronal loops. In what follows, we show only the saturation values.

Figure 3 shows how the axial phase speed $v_{\text{ph}} = \omega_{\text{R}}/k$ and damping-time-to-period ratio τ/P depend on the axial wavenumber k for a number of l/R as labeled. In addition to the results from the resistive computations (the solid lines), we also show the results found by solving the TB limit (dashed). The dash-dotted curve in Figure 3a shows what happens when $l/R = 0$. This corresponds to the case where the equilibrium parameters are transversely structured in a step-function fashion, and hence the label “step function”. Figure 3a shows that ω_{R}/k for $l/R \neq 0$ does not show a monotonical dependence on k as in the step-function case. Rather, ω_{R}/k decreases with k from the internal tube speed c_{Ti} , attains a local minimum, and then increases toward c_{Ti} again. This behavior is seen not only for the resistive results (the solid curves), but also for the TB ones (dashed). The latter behavior requires some explanation. In the case of weak damping, one usually proceeds by first solving the real part of the DR in the TB limit for ω_{R} , which is then used to find r_c such that ω_{I} can be found (see Y17 and references therein). With such an analytical approach, the TB results in Figure 3a will agree with the step-function case exactly. However, the nominal real part of the DR actually involves the complex-valued ω (see Equation 30 in Y17), and this turns out to have a subtle effect on the solutions. Indeed, Yu et al. (2017a) also went beyond the two-step procedure, and showed that the full numerical solution to the DR in the TB limit yields a nonmonotonical dependence of ω_{R}/k on k as well (Figure 5 therein). Note, however, that the equilibrium profiles adopted in Yu et al. (2017a) are different from ours and a direct comparison is not straightforward. What the dashed lines in our Figure 3a show is that the nonmonotonical behavior persists for our choice of the equilibrium profile in the TL.

Figure 3b is more relevant for examining how efficient resonant absorption may be to attenuate SSSMs. Examine the solid lines first, which pertain to the resistive computations. One sees that τ/P decreases first with kR but eventually increases again, and therefore for a chosen l/R there is an optimal axial wavenumber that maximizes wave attenuation. The

increase in τ/P at large kR occurs in conjunction with the tendency for the axial phase speed ω_R/k to approach c_{Ti} . Note that the $\tau/P - kR$ curve for a given l/R terminates when kR is sufficiently large. This does not mean that resonant SSSMs are prohibited for axial wavenumbers beyond some critical value. Rather, this comes from the issue that the eigenfrequencies still show some weak R_m dependence at the relevant kR even if we increase R_m to 10^{10} . The relevant values are therefore not presented because they do not meet our definition of “saturation”. This, however, is not really a physical issue given that the presented curves already allow us to show the existence of optimal axial wavenumbers. Comparing the solid with the dashed lines, one sees that the resistive computations yield a τ/P that can be considerably larger than its TB counterpart. Take $[l/R, kR] = [0.3, 2]$ for instance, in which case the resistive value $((\tau/P)_{\text{res}} = 680)$ is an order-of-magnitude larger than the TB one $((\tau/P)_{\text{TB}} = 39)$, despite that the TL is still rather narrow. One also sees that for a given l/R , the deviation of the resistive results from the TB ones becomes increasingly obvious when kR increases, or equivalently, when the axial wavelength $\lambda = 2\pi/k$ decreases. This is physically understandable because by “thin-boundary”, the layer width l should in principle be much smaller than the lengthscales in both the transverse (represented by R) and longitudinal (here represented by λ) directions.

Figure 4 examines the dispersive properties of SSSMs from another perspective, namely, how ω_R/k and τ/P depend on the dimensionless TL width l/R for a number of k as labeled. The results from the resistive computations (the solid curves) are also compared with the TB results (dashed). The comparison between the two sets of curves indicates that in general the TB limit overestimates wave damping, and becomes close to the resistive values only for relatively small l/R . Define $\epsilon = |(\tau/P)_{\text{res}}/(\tau/P)_{\text{TB}} - 1|$ for convenience. For a given kR , we also define $(l/R)_{\text{TB}}$ to be the value beyond which ϵ becomes $\gtrsim 30\%$. Then one finds that $(l/R)_{\text{TB}}$ decreases with kR , yielding 0.14 (0.05) for $kR = 0.3$ (2) for instance. In other words, $(l/R)_{\text{TB}}$ needs to be increasingly small when the axial wavelength decreases, as would have been intuitively expected.

Now examine only the solid curves. One finds from Figure 4 that the overall behavior of the axial phase speeds and damping-time-to-period ratios does not depend on the value of kR . Examine the blue solid curve in Figure 4a ($kR = 2$) for instance. One sees that ω_R/k tends to increase with l/R and eventually approaches c_{Ti} from below. We note that the curve terminates at $l/R \sim 0.3$, the reason being not that resonant SSSMs are prohibited thereafter. It is just that the eigenfrequencies do not saturate even at $R_m = 10^{10}$ and therefore their values are not presented. Moving on to Figure 4b, one sees that the blue solid curve shows a nonmonotonical dependence of τ/P on l/R , and there exists an optimal value of l/R that maximizes wave damping. Let $(\tau/P)_{\text{min}}$ denote the minimal τ/P that this curve attains and $(l/R)_{\text{min}}$ denote where the minimal value is reached. One sees also

that the tendency for τ/P to increase when $l/R > (l/R)_{\min}$ takes place when ω_R/k becomes sufficiently close to c_{Ti} (the blue solid curve in Figure 4a). In addition, both $(l/R)_{\min}$ and $(\tau/P)_{\min}$ seem to decrease monotonically with kR . This turns out to be indeed the case as shown by Figure 5, where we examine how $(l/R)_{\min}$ and $(\tau/P)_{\min}$ depend on kR for kR in the range between 0.7 and 4.3. Note that the tendency for $(\tau/P)_{\min}$ to decrease together with $(l/R)_{\min}$ when kR increases is not to be confused with the tendency for τ/P to increase with decreasing l/R when $(l/R) < (l/R)_{\min}$ for a given kR . The latter tendency is clear in Figure 4b, and is expected given that the cusp resonance will not take place in the extreme case when $l/R = 0$. What Figure 5 suggests is that τ/P is consistently larger than 110 for the adopted equilibrium parameters and the wavenumber range.

How do our results connect to the observations of SSSMs by G15? Actually what leads us to examine the particular range of kR in Figure 5 is based on G15 who examined an SSSM with an axial wavelength λ of 4400 km. If boldly assuming the same λ for SSSMs in photospheric pores in general, then one finds that $kR = 2\pi R/\lambda$ is in the range $[0.7, 4.3]$ with R ranging from 500 to 3000 km. Provided that this assumption holds and that our equilibrium parameters are representative of pores, then Figure 5 indicates that the cusp resonance is not efficient in damping SSSMs. To make Figure 4 more relevant to G15 where propagating rather than standing SSSMs are measured, we also computed the damping-length-to-wavelength ratio (L_D/λ) by connecting it to τ/P through the ratio of the axial group speed (v_{gr}) to the axial phase speed (v_{ph}) (see e.g., Terradas et al. 2010, Equation 40). This practice is justified because the damping we found is weak. It turns out that L_D/λ is nearly identical to τ/P because v_{gr}/v_{ph} differs little from unity, which in turn results from the extremely weak dispersion (see Figure 3a). The mean radius of the pore that G15 examined is ~ 1500 km, and consequently $kR \sim 2$. One reads from the blue solid curve in Figure 4b that τ/P (and hence L_D/λ) is no smaller than 180. We therefore conclude that with our chosen parameters, the cusp resonance is unlikely to account for the heavy spatial damping of the SSSM in G15, who found a value of $L_D/\lambda \sim 1/4$.

Let us come back to Figure 2. For any given pair of $[l/R, kR]$, three distinct intervals of the magnetic Reynolds number R_m show up as far as the behavior of τ/P is concerned. As has been discussed in substantial detail, the interval where τ/P shows no dependence on R_m corresponds to the case where only the cusp resonance operates to damp SSSMs. This happens for sufficiently large R_m . When R_m decreases, τ/P tends to experience an increasingly strong but still gradual dependence on R_m until a knee occurs (see the behavior of τ/P at $R_m \sim 10^5$ along the red dotted curve, for instance). Let this interval be called the intermediate regime. If further decreasing R_m beyond the knees, one sees that τ/P depends linearly on R_m , as would be expected if wave damping is solely determined by resistivity in the case of weak damping. In this case one expects that $|\omega_I| \propto \eta$, and consequently

$\tau = 1/|\omega_I| \propto 1/\eta \propto R_m$. That τ/P depends also linearly on R_m is because of the extremely weak R_m -dependence of ω_R and hence that of P . It is likely that when R_m decreases through the knee, the resonant SSSM transitions to an ordinary resistive slow mode. We conjecture this by drawing analogy to resonant kink modes in typical coronal loops. In that case, resonant kink modes cannot be told apart from ordinary resistive Alfvén modes when the loop boundary becomes sufficiently thick (see Fig. 2 in [Van Doorselaere & Poedts 2007](#) for slab computations; and Fig. 8 in [Arregui et al. 2005](#) for cylindrical computations). However, there is one important difference: the SSSMs remain weakly damped in this study, whereas the kink modes are heavily damped in the coronal studies. It therefore remains open as to why the dependence of τ/P on resistivity becomes qualitatively different when R_m crosses the knee. We stress that this behavior is not a numerical artifact, because it persists even though we have experimented with different choices of grid spacing and different trajectories that lead to a given $[l/R, kR, R_m]$ in this three-dimensional parameter space.

Now focus on the red curves, which pertain to $kR = 2$ and therefore are directly relevant to G15. As mentioned in Section 1, we quote the range of electric conductivity as given by [Kovitya & Cram \(1983, Table 2\)](#). For a pore with radius $R \sim 1500$ km and the adopted equilibrium parameters, R_m ranges from 3×10^4 to 10^7 as given by the area shaded green. One sees that the majority of this range lies in the intermediate regime where both resistivity and the cusp resonance play a role in damping the SSSM in question. When $R_m = 10^7$, the cusp resonance is nearly the sole factor that damps the SSSM for $l/R = 0.1$ (the solid red curve), whereas resistivity is still important to some extent for $l/R = 0.3$ (dotted). On the contrary, when $R_m = 3 \times 10^4$, the cusp resonance still plays some role in wave damping for $l/R = 0.1$, whereas wave damping is entirely due to resistivity for $l/R = 0.3$. Regardless, τ/P at this lower bound is substantially smaller than the values due to the cusp resonance alone. Take $l/R = 0.3$ for instance, for which one finds that τ/P reads 28.9 when $R_m = 3 \times 10^4$ but 529 when $R_m = 10^7$. It is therefore safe to conclude that resistivity should be taken into account when the damping of SSSMs in photospheric pores is examined. However, literally translating τ/P to L_D/λ , one finds that the derived damping-length-to-wavelength ratio is still quite far from the value found by G15.

4. SUMMARY AND CONCLUDING REMARKS

This study has been motivated by the considerable interest in sausage modes in photospheric waveguides, and the spatial damping of propagating slow surface sausage modes (SSSMs) as examined by [Grant et al. \(2015, G15\)](#) in particular. Working in the framework of linear resistive MHD, we examined the effects of resistivity and resonant coupling to the cusp

continuum on the damping of SSSMs in a photospheric cylinder, for which the transverse structuring comprises a uniform cord, a uniform exterior, and a continuous transition layer (TL) in between. We found that in general the damping due to the cusp resonance alone is rather weak, with the minimal damping-time-to-period ratio (and hence the damping-length-to-wavelength ratio) reaching a value of the order 100. However, resistivity can be an order-of-magnitude more efficient, making it an indispensable ingredient for examining the damping of SSSMs.

Regarding the cusp resonance, the full numerical approach allowed us to examine TLs of arbitrary width, and hence allowed a comparison with the TB limit where the TL width is assumed to be small. We found that for the equilibrium parameters we examine, the constraint on the range of applicability of the TB approximation is rather stringent. Relevant to G15 for which the dimensionless axial wavenumber $kR \sim 2$, we find that the TL width in units of the waveguide radius (l/R) needs to be $\lesssim 0.05$ for the TB results to be accurate within 30%. The TB results tend to overestimate wave damping, by an order-of-magnitude when $l/R = 0.3$.

Our study suggests that neither the cusp resonance nor electric resistivity can account for the heavy spatial damping of the SSSM measured by G15. However, this is not the end of the story. As shown by [Yu et al. \(2017a\)](#), the damping efficiency due to the cusp resonance may be sensitive to the detailed form of the transverse distribution of the equilibrium parameters. On top of that, the values of the equilibrium parameters themselves are expected to be important as well. Our study on the cusp resonance has not exhausted neither of these two options; rather, we adopted a particular transverse profile and a given set of equilibrium parameters. Furthermore, the resistivity we examined only accounted for electron-ion and electron-neutral collisions ([Kovitya & Cram 1983](#)). However, the temperature in the photospheric portion of the pore examined by G15 may be ~ 3500 K, meaning that the ionization degree is likely to be very low. The Cowling resistivity resulting from ion-neutral collisions may be substantially stronger than the Ohmic resistivity we examined. While the Cowling resistivity has been examined in the wave context for, e.g., kink modes resonantly coupled to the Alfvén continuum in prominence threads ([Soler et al. 2009](#)), its effect on the damping of SSSMs in photospheric waveguides has yet to be assessed. A study along this line of thinking is underway, and seismological applications are being explored to infer such parameters as the transverse lengthscales and the strengths of both the Ohmic and ambipolar diffusivities.

We thank the referee for his/her constructive comments. We thank Tom Van Doorselaere for carefully reading the first draft. This work is supported by the National Natural Science Foundation of China (41474149, 41604145, 41674172, 11761141002, 41704165), and by the Provincial Natural Science Foundation of Shandong via Grant ZR2016DP03 (HY).

REFERENCES

- Arregui, I. 2015, *Philosophical Transactions of the Royal Society of London Series A*, 373, 20140261
- Arregui, I., Oliver, R., & Ballester, J. L. 2012, *Living Reviews in Solar Physics*, 9, 2
- Arregui, I., Van Doorselaere, T., Andries, J., Goossens, M., & Kimpe, D. 2005, *A&A*, 441, 361
- Aschwanden, M. J., Fletcher, L., Schrijver, C. J., & Alexander, D. 1999, *ApJ*, 520, 880
- Aschwanden, M. J. & Schrijver, C. J. 2011, *ApJ*, 736, 102
- De Moortel, I. & Browning, P. 2015, *Philosophical Transactions of the Royal Society of London Series A*, 373, 20140269
- De Moortel, I. & Nakariakov, V. M. 2012, *Philosophical Transactions of the Royal Society of London Series A*, 370, 3193
- De Pontieu, B., McIntosh, S. W., Carlsson, M., Hansteen, V. H., Tarbell, T. D., Schrijver, C. J., Title, A. M., Shine, R. A., Tsuneta, S., Katsukawa, Y., Ichimoto, K., Suematsu, Y., Shimizu, T., & Nagata, S. 2007, *Science*, 318, 1574
- Dorotovič, I., Erdélyi, R., Freij, N., Karlovský, V., & Márquez, I. 2014, *A&A*, 563, A12
- Dorotovič, I., Erdélyi, R., & Karlovský, V. 2008, in *IAU Symposium, Vol. 247, Waves & Oscillations in the Solar Atmosphere: Heating and Magneto-Seismology*, ed. R. Erdélyi & C. A. Mendoza-Briceno, 351–354
- Edwin, P. M. & Roberts, B. 1983, *Sol. Phys.*, 88, 179
- Erdélyi, R. & Taroyan, Y. 2008, *A&A*, 489, L49
- Freij, N., Dorotovič, I., Morton, R. J., Ruderman, M. S., Karlovský, V., & Erdélyi, R. 2016, *ApJ*, 817, 44
- Goossens, M., Erdélyi, R., & Ruderman, M. S. 2011, *Space Sci. Rev.*, 158, 289
- Grant, S. D. T., Jess, D. B., Moreels, M. G., Morton, R. J., Christian, D. J., Giagkiozis, I., Verth, G., Fedun, V., Keys, P. H., Van Doorselaere, T., & Erdélyi, R. 2015, *ApJ*, 806, 132
- Guo, M.-Z., Chen, S.-X., Li, B., Xia, L.-D., & Yu, H. 2016, *Sol. Phys.*, 291, 877

- He, J., Marsch, E., Tu, C., & Tian, H. 2009, *ApJ*, 705, L217
- Jess, D. B., Mathioudakis, M., Christian, D. J., Keenan, F. P., Ryans, R. S. I., & Crockett, P. J. 2010, *Sol. Phys.*, 261, 363
- Jess, D. B., Mathioudakis, M., Erdélyi, R., Crockett, P. J., Keenan, F. P., & Christian, D. J. 2009, *Science*, 323, 1582
- Jess, D. B., Van Doorselaere, T., Verth, G., Fedun, V., Krishna Prasad, S., Erdélyi, R., Keys, P. H., Grant, S. D. T., Uitenbroek, H., & Christian, D. J. 2017, *ApJ*, 842, 59
- Keys, P. H., Morton, R. J., Jess, D. B., Verth, G., Grant, S. D. T., Mathioudakis, M., Mackay, D. H., Doyle, J. G., Christian, D. J., Keenan, F. P., & Erdélyi, R. 2018, *ApJ*, 857, 28
- Khomenko, E. & Collados, M. 2012, *ApJ*, 747, 87
- Kovitya, P. & Cram, L. 1983, *Sol. Phys.*, 84, 45
- Moreels, M. G., Freij, N., Erdélyi, R., Van Doorselaere, T., & Verth, G. 2015, *A&A*, 579, A73
- Morton, R. J., Erdélyi, R., Jess, D. B., & Mathioudakis, M. 2011, *ApJ*, 729, L18
- Morton, R. J., Verth, G., Jess, D. B., Kuridze, D., Ruderman, M. S., Mathioudakis, M., & Erdélyi, R. 2012, *Nature Communications*, 3, 1315
- Nakariakov, V. M., Ofman, L., Deluca, E. E., Roberts, B., & Davila, J. M. 1999, *Science*, 285, 862
- Nakariakov, V. M., Pilipenko, V., Heilig, B., Jelínek, P., Karlický, M., Klimushkin, D. Y., Kolotkov, D. Y., Lee, D.-H., Nisticò, G., Van Doorselaere, T., Verth, G., & Zimovets, I. V. 2016, *Space Sci. Rev.*, 200, 75
- Nakariakov, V. M. & Verwichte, E. 2005, *Living Reviews in Solar Physics*, 2, 3
- Ni, L., Lin, J., Roussev, I. I., & Schmieder, B. 2016, *ApJ*, 832, 195
- Ofman, L. & Wang, T. J. 2008, *A&A*, 482, L9
- Pascoe, D. J., Goddard, C. R., & Nakariakov, V. M. 2016, *A&A*, 593, A53
- Poedts, S. & Kerner, W. 1991, *Physical Review Letters*, 66, 2871

- Sewell, G. 1988, *The Numerical Solution of Ordinary and Partial Differential Equations* (San Diego: Academic Press)
- Soler, R., Goossens, M., Terradas, J., & Oliver, R. 2013, *ApJ*, 777, 158
- Soler, R., Oliver, R., & Ballester, J. L. 2009, *ApJ*, 707, 662
- Terradas, J., Goossens, M., & Verth, G. 2010, *A&A*, 524, A23
- Terradas, J., Oliver, R., & Ballester, J. L. 2006, *ApJ*, 642, 533
- Tian, H., DeLuca, E. E., Cranmer, S. R., De Pontieu, B., Peter, H., Martínez-Sykora, J., Golub, L., McKillop, S., Reeves, K. K., Miralles, M. P., McCauley, P., Saar, S., Testa, P., Weber, M., Murphy, N., Lemen, J., Title, A., Boerner, P., Hurlburt, N., Tarbell, T. D., Wuelser, J. P., Kleint, L., Kankelborg, C., Jaeggli, S., Carlsson, M., Hansteen, V., & McIntosh, S. W. 2014, *Science*, 346, 1255711
- Van Doorselaere, T., Andries, J., Poedts, S., & Goossens, M. 2004, *ApJ*, 606, 1223
- Van Doorselaere, T. & Poedts, S. 2007, *Plasma Physics and Controlled Fusion*, 49, 261
- Verwichte, E., Aschwanden, M. J., Van Doorselaere, T., Foullon, C., & Nakariakov, V. M. 2009, *ApJ*, 698, 397
- Wang, F., Deng, H., Li, B., Feng, S., Bai, X., Deng, L., Yang, Y., Xue, Z., & Wang, R. 2018, *ApJ*, 856, L16
- Wang, J. 1993, in *Astronomical Society of the Pacific Conference Series*, Vol. 46, IAU Colloq. 141: *The Magnetic and Velocity Fields of Solar Active Regions*, ed. H. Zirin, G. Ai, & H. Wang, 465
- Wang, T., Solanki, S. K., Curdt, W., Innes, D. E., & Dammasch, I. E. 2002, *ApJ*, 574, L101
- Yu, D. J., Van Doorselaere, T., & Goossens, M. 2017a, *ApJ*, 850, 44
- . 2017b, *A&A*, 602, A108

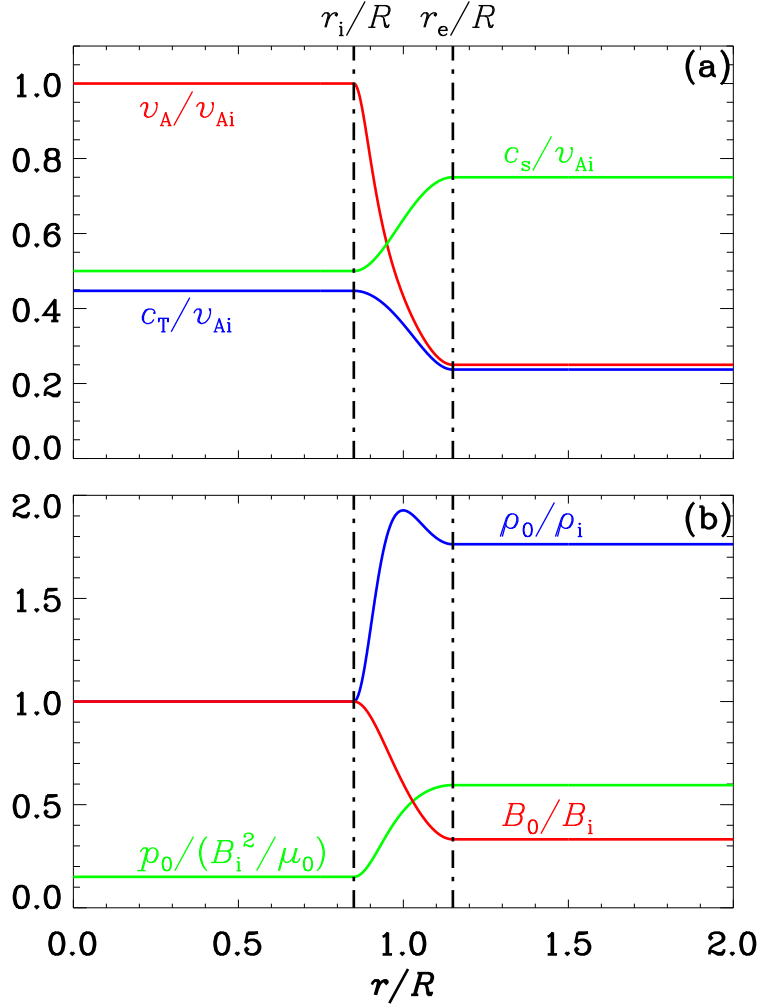


Fig. 1.— Transverse profiles for the equilibrium parameters of a photospheric waveguide representative of a pore. Both the characteristic speeds (the upper panel) and equilibrium fluid parameters (lower) are shown. Characteristic of these profiles is that a continuous transition layer (TL) connects a uniform cord and a uniform exterior. This TL is located between $r_i = R - l/2$ and $r_e = R + l/2$, where R is the mean waveguide radius and l the TL width. Here l/R is arbitrarily chosen to be 0.3 for illustration purposes.

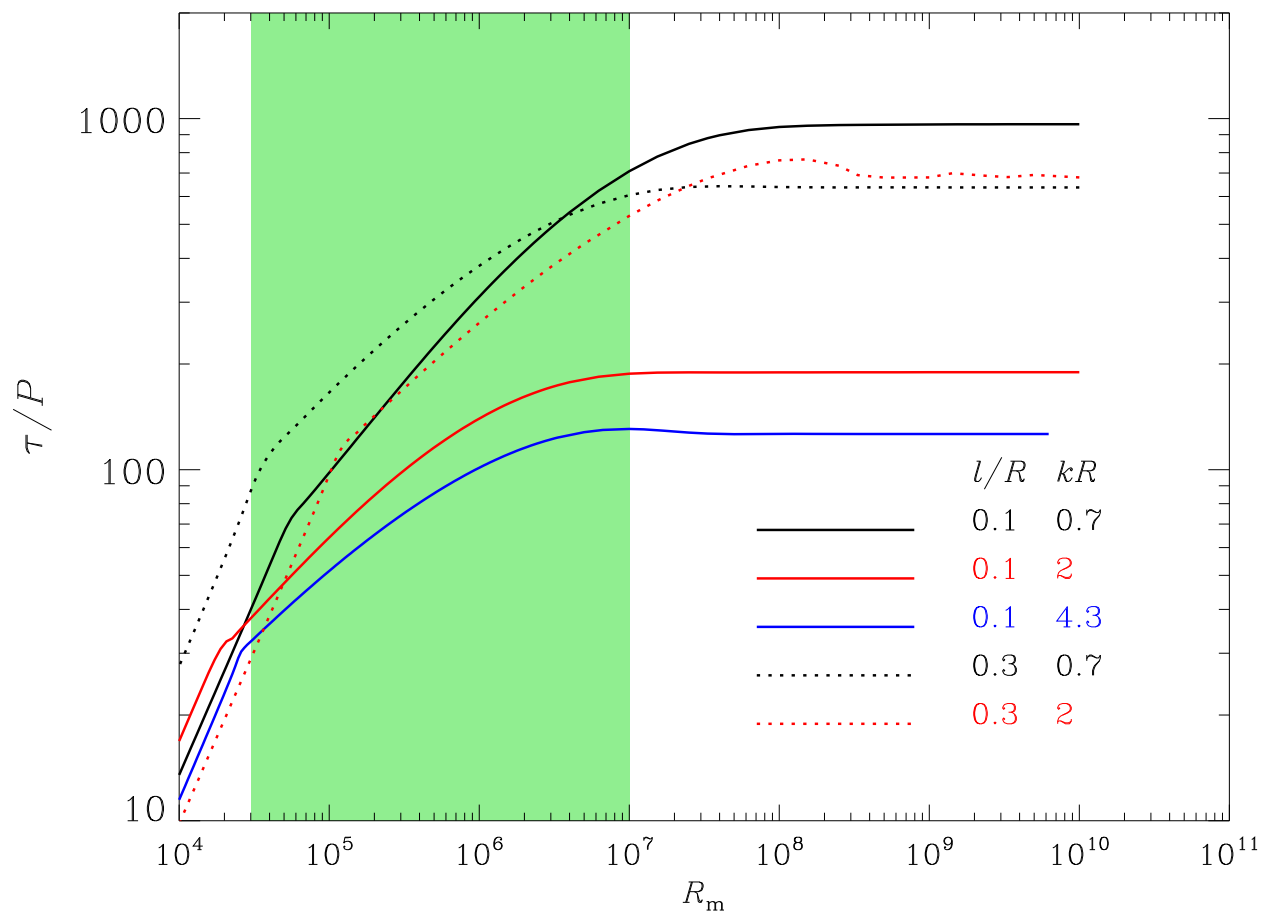


Fig. 2.— Dependence on the magnetic Reynolds number (R_m) of the damping-time-to-period ratio (τ/P) of slow surface sausage modes in a photospheric waveguide representative of a pore. A number of combinations of the transition layer width l and axial wavenumber k are examined as labeled. The area shaded green corresponds to the range of R_m derived from accepted values of electric conductivity. See text for details.

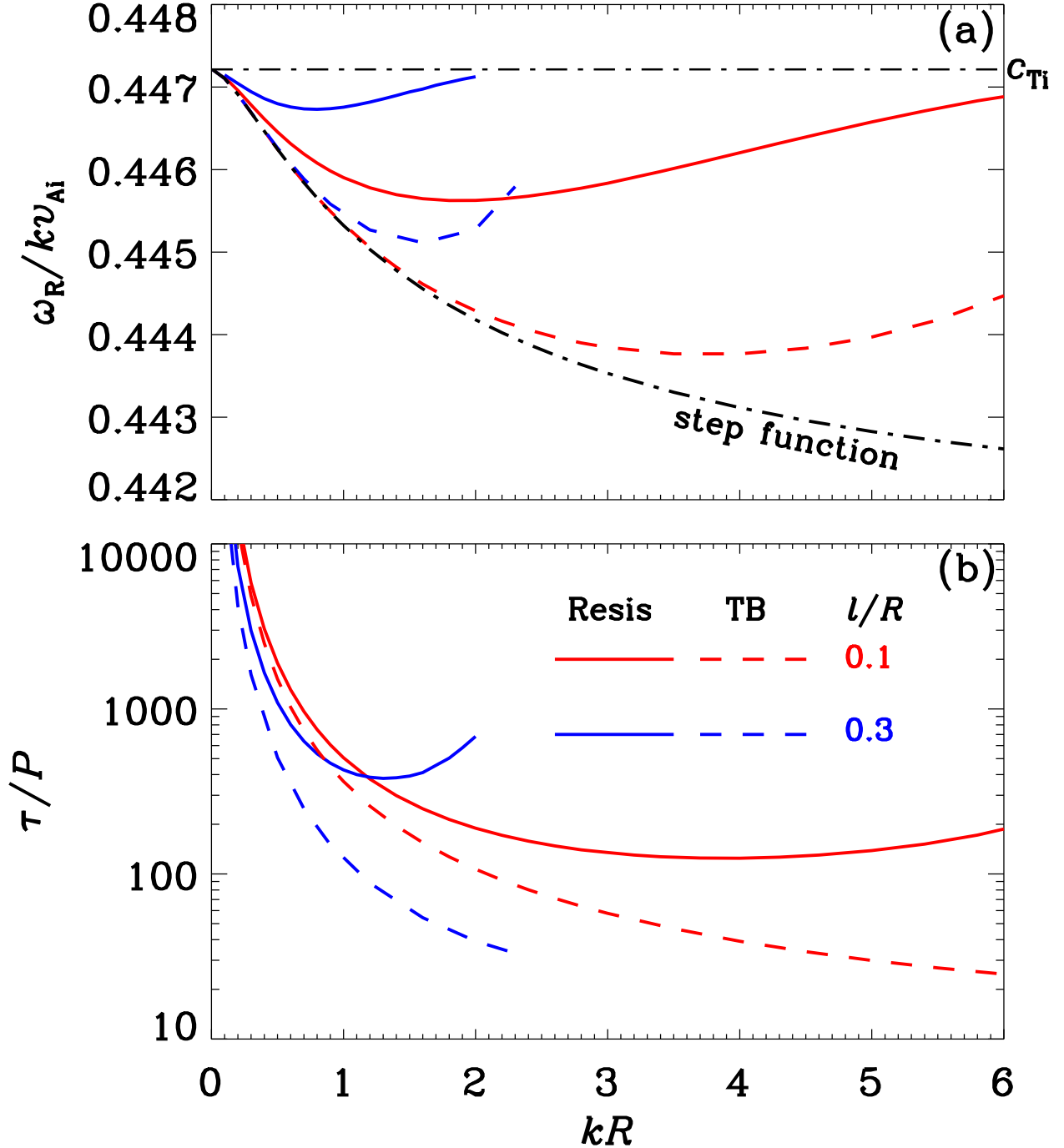


Fig. 3.— Dispersive properties of slow surface sausage modes resonantly coupled to the cusp continuum, shown by the dependence on the axial wavenumber (k) of (a) the axial phase speed ($\omega_R/(k v_{Ai})$) and (b) the damping-time-to-period ratio (τ/P). Two values of the transition layer width l (in units of the mean waveguide radius R) are presented by the lines with different colors as labeled. In addition to the results from our resistive computations (the solid curves), those from the thin-boundary (TB) computations are also shown (dashed). The black dash-dotted curve in panel (a) corresponds to the case where $l/R = 0$, namely the equilibrium parameters are transversely structured as a step function.

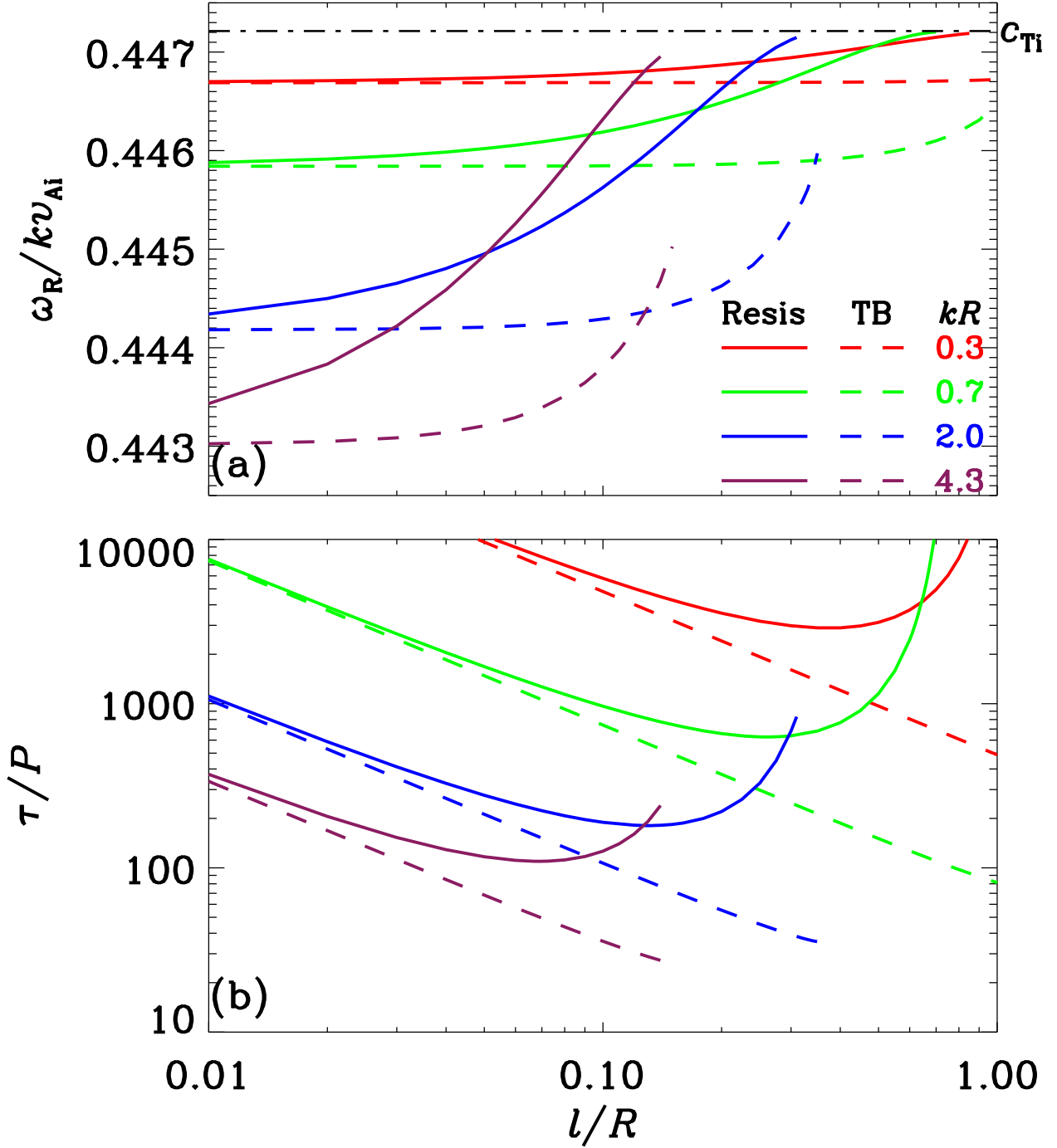


Fig. 4.— Dispersive properties of slow surface sausage modes resonantly coupled to the cusp continuum, shown by the dependence on the dimensionless layer width (l/R) of (a) the axial phase speed ($\omega_R/(k v_{Ai})$) and (b) the damping-time-to-period ratio (τ/P). A number of values of the axial wavenumber kR are presented by the lines with different colors as labeled. In addition to the results from our resistive computations (the solid curves), those from the thin-boundary (TB) computations are also shown (dashed).

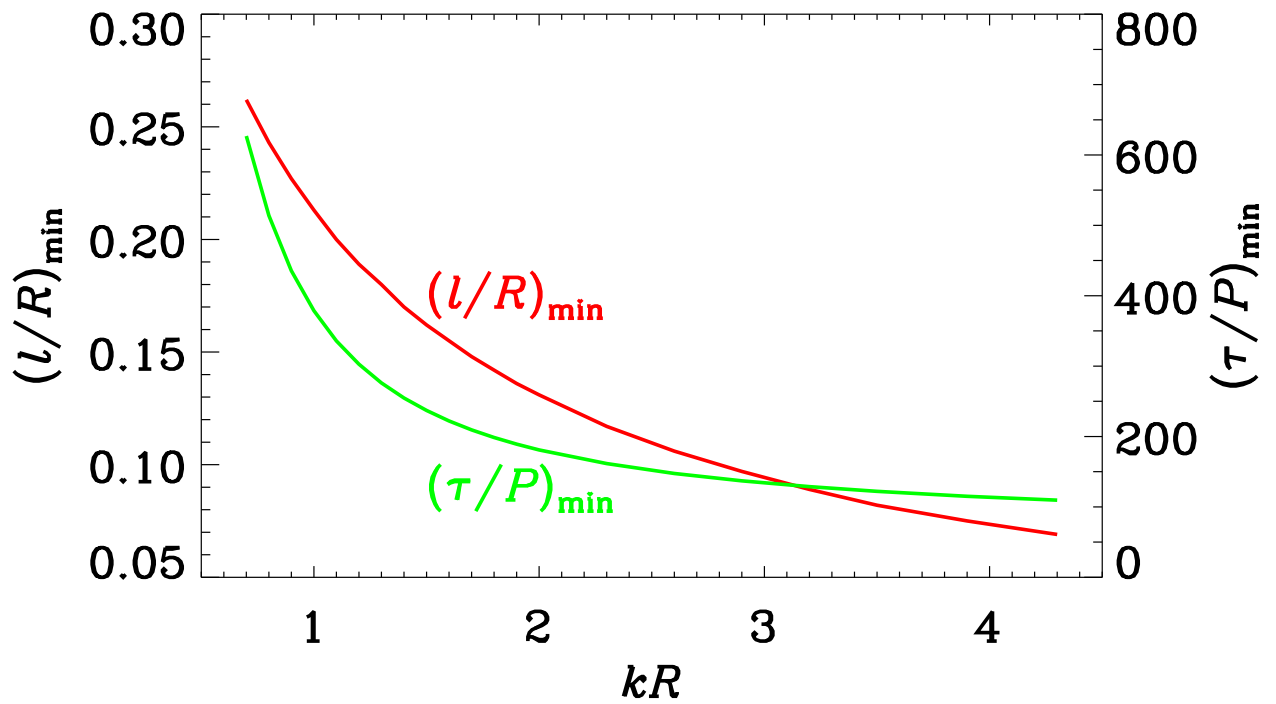


Fig. 5.— Dependence on the axial wavenumber (k) of the optimal damping-time-to-period ratio $((\tau/P)_{\min})$ and the dimensionless transition layer width $((l/R)_{\min})$ where the optimal damping is reached. See text for details.